LETTERS
PUBLISHED ONLINE: 13 FEBRUARY 2017 | DOI: 10.1038/NMAT4855
nature materials

A magnetic heterostructure of topological insulators as a candidate for an axion insulator

M. Mogi[1*†], M. Kawamura[2†], R. Yoshimi[2], A. Tsukazaki[3], Y. Kozuka[1], N. Shirakawa[4], K. S. Takahashi[2,5], M. Kawasaki[1,2] and Y. Tokura[1,2*]

The axion insulator which may exhibit an exotic quantized magnetoelectric effect[1–6] is one of the most interesting quantum phases predicted for the three-dimensional topological insulator (TI). The axion insulator state is expected to show up in magnetically doped TIs with magnetizations pointing inwards and outwards from the respective surfaces. Towards the realization of the axion insulator, we here engineered a TI heterostructure in which magnetic ions (Cr) are modulation-doped only in the vicinity of the top and bottom surfaces of the TI ($(Bi,Sb)_2Te_3$) film[7]. A separation layer between the two magnetic layers weakens interlayer coupling between them, enabling the magnetization reversal of individual layers. We demonstrate the realization of the axion insulator by observing a zero Hall plateau (ZHP) (where both the Hall and longitudinal conductivity become zero) in the electric transport properties, excluding the other possible origins for the ZHP[8–10]. The manifestation of the axion insulator can lead to a new stage of research on novel magnetoelectric responses in topological matter.

Topological aspects and related electronic phenomena of condensed matter have been one of the central topics in contemporary materials science. A three-dimensional (3D) topological insulator (TI) realized in such materials as strained-HgTe[11], $Bi_{2-x}Sb_xTe_{3-y}Se_y$ (ref. 12), and $(Bi,Sb)_2Te_3$ (ref. 13), having an insulating bulk state and a metallic topological surface state[1,2], can provide a simple and ideal laboratory to study non-trivial phenomena arising from the topology of the materials. The quantum anomalous Hall (QAH) effect[14] is one such example as observed in magnetically doped topological insulators (MTIs)[15–17]. Because of the exchange interaction between the surface electrons and the magnetic moments, the ferromagnetic moment perpendicular to the surface opens a gap on the surface state, leaving a gapless one-dimensional chiral edge channel (Fig. 1a). As a result, the Hall conductance is quantized to e^2/h when the Fermi energy resides in the magnetization gap. Theoretically, the QAH effect is viewed as one of the consequences of a quantized magnetoelectric coupling term known as the axion term[3–6].

The topological magnetoelectric (TME) effect is another quantization phenomenon predicted theoretically to arise from the axion term[3–6]. Magnetization can be induced by applying an electric field, and electric polarization by applying a magnetic field, with a magnetoelectric susceptibility given by the fine structure constant ($\alpha \sim 1/137$). A special configuration of the magnetization is required to observe the TME effect; the magnetizations should point inwards or outwards from the surface so that all the surfaces of the surrounding the 3D TI are gapped and the 3D TI becomes an insulator, termed as an axion insulator[3,5,6]. However, experimental observation of the TME effect remains unexplored because of difficulties in realizing the axion insulator state.

In the case of thin-film geometry, the above condition of the inward or outward magnetization is fulfilled with the anti-parallel magnetization alignment of the top and bottom surfaces, as shown in Fig. 1b; namely magnetizations are to point up on the top surface and point down on the bottom surface[18,19]. In addition to the gap opening at the top and bottom surfaces by the perpendicular magnetization, the side surface is also gapped due to the quantum confinement effect[20,21]. Thus, all the surface states are gapped to form an axion insulator with vanishing Hall conductivity (σ_{xy}) and longitudinal conductivity (σ_{xx}). Recent theories have shown that the TME effect can occur in such a thin film with a quantum confinement gap when the magnetizations are anti-parallel to each other[18,19]. Accordingly, control of magnetism in the 3D MTI thin films provides an important key to the realization of the axion insulator.

To realize the anti-parallel magnetization on the top and bottom surfaces of the 3D MTI, we engineered magnetic heterostructures of Cr-doped $(Bi,Sb)_2Te_3$ (BST) thin films by using the layer-by-layer growth of molecular beam epitaxy. We doped Cr (12%) selectively to 2-nm-thick layers in the vicinity of the top and bottom surfaces, as shown in Fig. 1d, so that the surface electrons on the top (bottom) surface mainly and strongly interact with the upper (lower)Cr-doped layer through the exchange interaction. Such a modulation doping of magnetic moments enhances the stability of the QAH state up to several kelvin (see Supplementary Note 1 and ref. 7). Here, as a new attempt, a vertical asymmetry is introduced to the heterostructure; the bottom Cr-doped BST layer is 1 nm away from the bottom surface, while the top Cr-doped BST layer is in contact with the top surface. The asymmetry leads to different coercive fields (B_c) in the two layers. Furthermore, we make sure that the BST separation layer (5 nm) between Cr-doped BST layers has enough thickness to reduce the interlayer coupling. The total film thickness of 10 nm can also weaken the coupling between the top and bottom surface states[22,23]. For the control experiments, we also prepared a vertically symmetric MTI heterostructure film with a thinner BST separation layer (2 nm) (Fig. 1d) and an 8-nm-thick homogeneously Cr(5%)-doped $(Bi_{0.22}Sb_{0.78})_2Te_3$ single-layer film (Fig. 1c) (see Methods for the film growth and Supplementary Note 2 of cross-sectional analysis of the heterostructure).

[1]Department of Applied Physics and Quantum Phase Electronics Center (QPEC), University of Tokyo, Bunkyo-ku, Tokyo 113-8656, Japan. [2]RIKEN Center for Emergent Matter Science (CEMS), Wako, Saitama 351-0198, Japan. [3]Institute for Materials Research, Tohoku University, Sendai, Miyagi 980-8577, Japan. [4]Flexible Electronics Research Center, National Institute of Advanced Industrial Science and Technology (AIST), Tsukuba, Ibaraki 305-8565, Japan. [5]PRESTO, Japan Science and Technology Agency (JST), Chiyoda-ku, Tokyo 102-0075, Japan. †These authors contributed equally to this work.
*e-mail: mogi@cmr.t.u-tokyo.ac.jp; tokura@riken.jp

© 2017 Macmillan Publishers Limited, part of Springer Nature. All rights reserved.

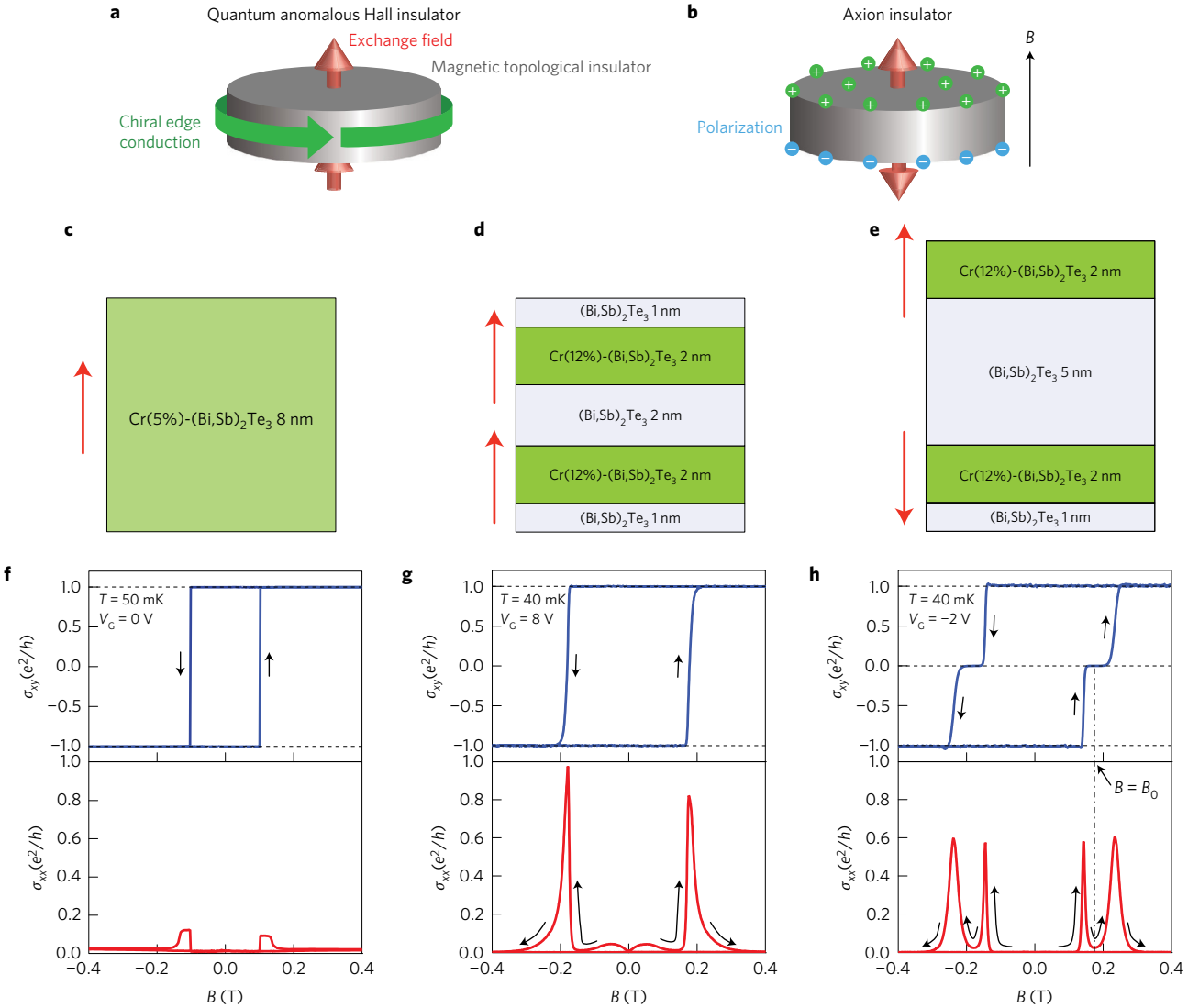

Figure 1 | ZHP state in a MTI heterostructure towards an axion insulator. a,**b**, Schematic drawings of a quantum anomalous Hall (QAH) insulator (**a**) and an axion insulator (**b**) in magnetic TI thin films. In an axion insulator, a magnetic field induces electric polarization and an electric field induces magnetization as the TME effect. **c**–**e**, Schematic layouts of MBE-grown Cr-modulation-doped TI ($(Bi,Sb)_2Te_3$) thin films used for the experiments. The Cr density (%) and Bi:Sb ratio of respective films are 5%, 22:78 (**c**) and 12%, 26:74 (**d**,**e**). **f**–**h**, Magnetic field (B) dependence of Hall conductivity (σ_{xy}) and longitudinal conductivity (σ_{xx}) at the lowest temperature (40–50 mK) of a dilution refrigerator in the respective thin films shown in **c**–**e**. The applied gate voltage is fixed at charge neutrality of the respective thin films ($V_G = 0$ V for **c**, 8 V for **d**, −2 V for **e**). The measured range of B is between 2 T and −2 T for magnetization training. B taking a minimal value of σ_{xx} in the ZHP state is defined as $B = B_0$.

In terms of magnetotransport measurements, we can verify the realization of the QAH state and an axion insulator depending on the magnetization direction of two magnetic layers in the MTI heterostructure. When the applied perpendicular magnetic field (B) is large enough to align the magnetizations of the two magnetic layers parallel, then the QAH state with $\sigma_{xy} = e^2/h$ is expected to appear. With decreasing magnetic field close to B_c, the magnetization of one of the Cr-doped layers is reversed to form the anti-parallel magnetization alignment, as shown in Fig. 1b, which can host the axion insulator with $\sigma_{xy} = 0$. With further decrease in magnetic field, the magnetization of the other Cr-doped layer is also reversed and the magnetizations become parallel again, returning to the QAH state. Thus, by monitoring the magnetic field dependence of σ_{xy}, the emergence of the axion insulator can be observed. For the transport measurement, we prepared Hall-bar and Corbino-disk devices with electrostatic gates to tune the Fermi energy in the magnetization gap. These devices were cooled using a dilution refrigerator, and the longitudinal and Hall resistances were measured using a standard lock-in technique (see Methods for the device fabrication and measurement set-up).

Let us begin with the results of the homogeneously Cr-doped 8-nm-thick film (Fig. 1c). The QAH state is exhibited with σ_{xy} quantized to $\pm e^2/h$ and almost vanishing σ_{xx} at $B = 0$ T (Fig. 1f). σ_{xy} transits between $+e^2/h$ and $-e^2/h$, sharply accompanied by a single peak in σ_{xx}. This result indicates that the magnetization reversal of the MTI occurs at once at the single coercive field B_c. Similarly, in the symmetric MTI heterostructure (Fig. 1d), quantized σ_{xy} reverses sharply accompanied by a single peak in σ_{xx} at around $B = B_c$ (Fig. 1g), indicating that the magnetization reversal of the two magnetic layers occurs simultaneously at a single B_c. We infer that the two magnetic layers happen to have the same B_c and/or that an interlayer magnetic coupling between them remains more or less because of the relatively thin separation layer (2 nm).

In contrast to the above results, in the asymmetric MTI heterostructure (Fig. 1e), we observe clear zero Hall conductivity

© 2017 Macmillan Publishers Limited, part of Springer Nature. All rights reserved.

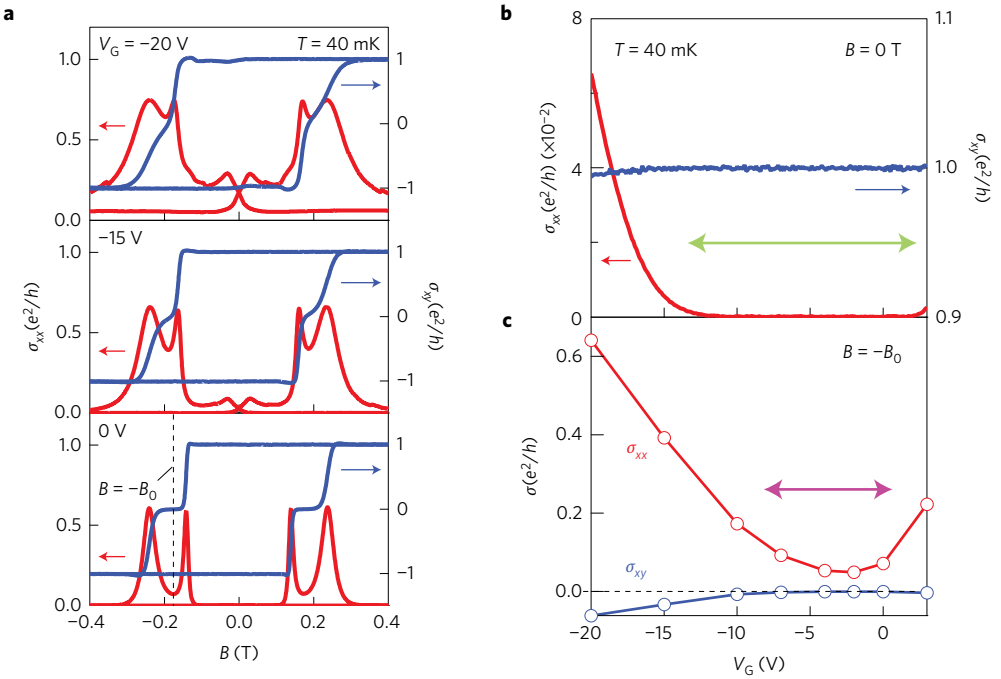

Figure 2 | Comparison between ZHP and QAH states in gate voltage dependence. a, Magnetic field (B) dependence of Hall conductivity (σ_{xy}) and longitudinal conductivity (σ_{xx}) in the asymmetrically Cr-doped thin films (Fig. 1e) at various gate voltages, $V_G = 0, -15$ and -20 V at $T = 40$ mK. **b**,**c**, Gate voltage (V_G) dependence for the quantum anomalous Hall state at $B = 0$ T after training of magnetization by applying $B = 2$ T (**b**) and for the ZHP state at $B = -B_0$ (**c**) plotted from the B scan data of σ_{xy}. Double-headed arrows in **b** (green) and **c** (purple) are guides to the eyes for the V_G width sustaining the QAH and ZHP states, respectively.

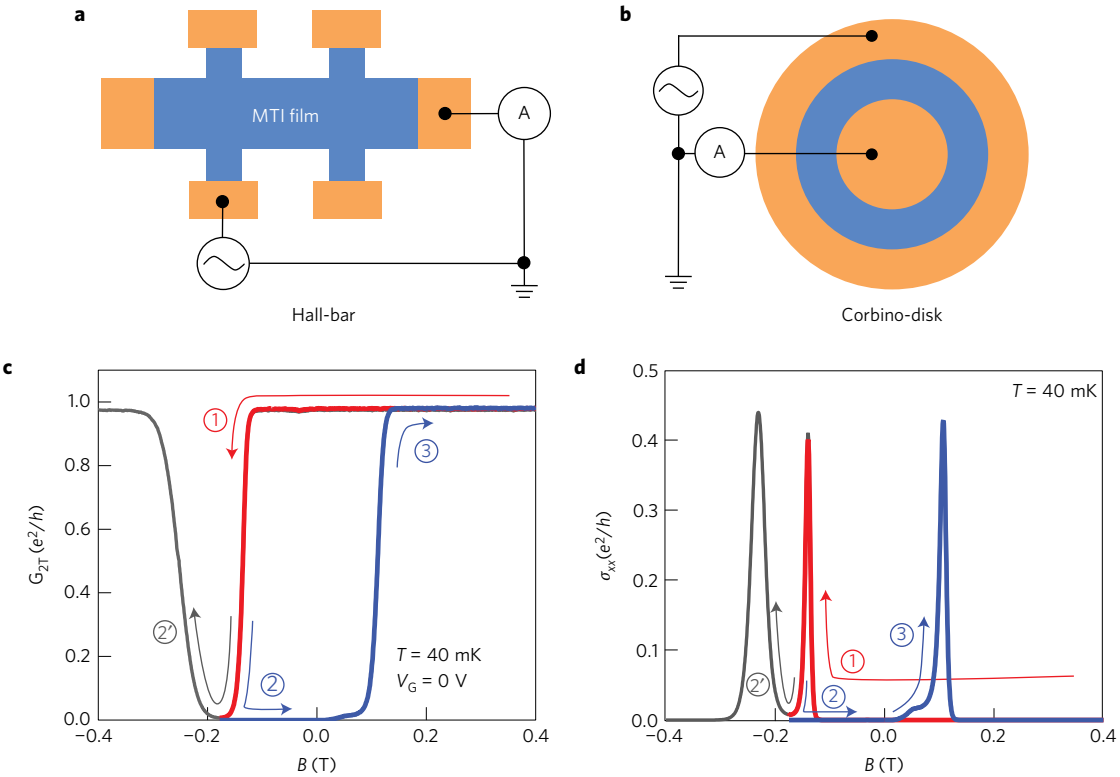

Figure 3 | Zero longitudinal conductivity and the persistence at zero magnetic field in the ZHP state. a,**b**, Schematic illustration of the two-terminal conductivity measurement in a Hall-bar geometry (**a**) and a Corbino-disk geometry (**b**) by applying a 10-μV a.c. voltage. **c**,**d**, Two-terminal conductivity (G_{2T}) (**c**) and longitudinal conductivity (σ_{xx}) (**d**) as a function of magnetic field (B) of the minor loop (from red line to blue line) and the full loop from $B = 2$ T to -2 T (from red line to grey line) at $T = 40$ mK without applying a gate voltage. The arrows and the numbers are guides to the eyes representing the direction and sequence of the field scan. The value of σ_{xx} is calculated by the relation: $\sigma_{xx} = 2\pi\sigma_0 \ln(r_{out}/r_{in})$, where σ_0 represents a measured conductance and r_{out} (r_{in}) represents the outer (inner) radius of the Corbino-disk.

© 2017 Macmillan Publishers Limited, part of Springer Nature. All rights reserved.

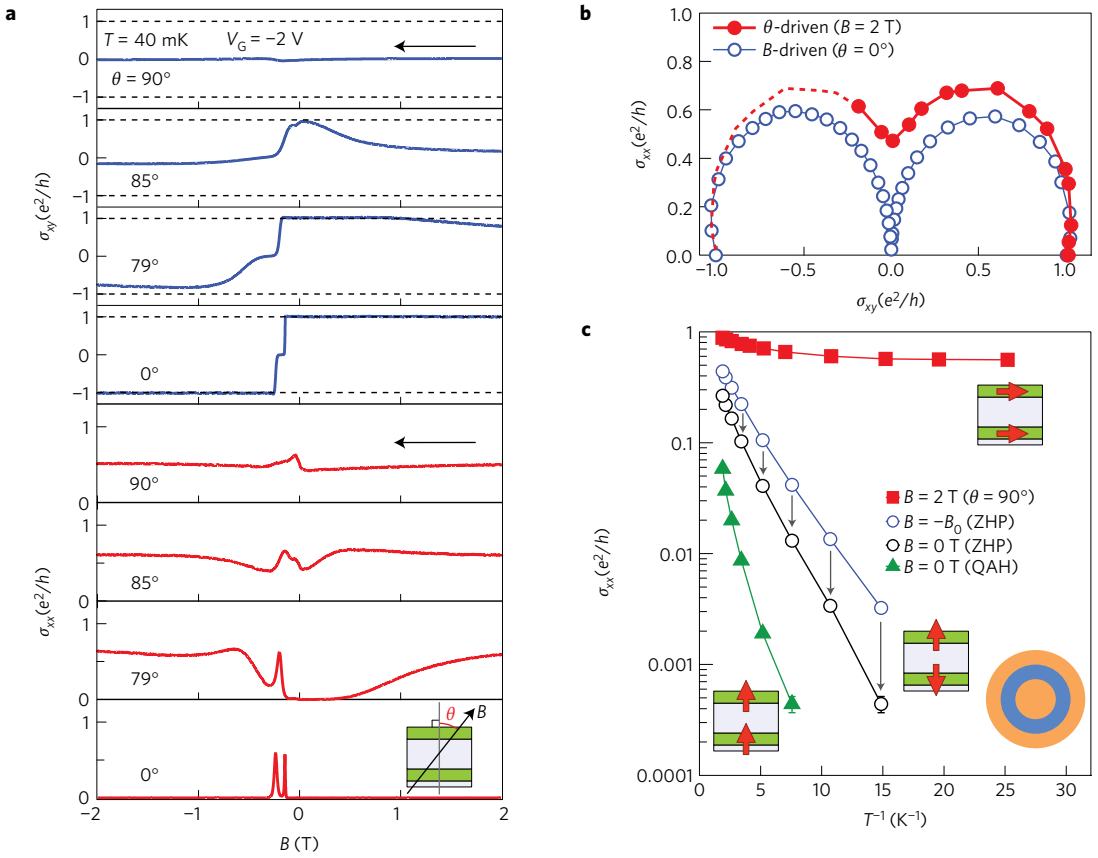

Figure 4 | Conductivity under various magnetization alignments. a, Magnetic field (B) (swept from 2 T to −2 T) dependence of Hall conductivity (σ_{xy}) and longitudinal conductivity (σ_{xx}) when under field angles $\theta = 0°$, 79°, 85°, 90° at $T = 40$ mK and $V_G = -2$ V in the Hall-bar geometry. θ is defined as the angle off the normal of the film. **b**, Comparison between (σ_{xy}, σ_{xx})-plots by the magnetic-field-driven results at $\theta = 0°$ (out-of-plane) (blue open circles) and the θ-driven (from 0 to 96°) (red solid circles) results at $B = 2$ T. The θ-driven curve is symmetrized and connected by a dashed line from the results between 0 and 96°. **c**, Temperature ($T = 530$, 470, 380, 300, 200, 130, 90, 70 and 40 mK) dependence of σ_{xx} under the QAH and ZHP states and under an in-plane magnetic field ($B = 2$ T) on a logarithmic scale as a function of $1/T$. Red solid squares show the data of σ_{xx} under an in-plane magnetic field. Blue and black open circles show σ_{xx} under ZHP state at $B = -B_0$ and 0 T respectively. Green solid triangles show σ_{xx} under QAH state at $B = 0$ T. The data are taken in the Corbino-disk geometry (as in Fig. 3c). On lowering the temperature, σ_{xx} in the ZHP state (~40 mK) and the QAH state (~100 mK) becomes smaller than 0.0002 e^2/h.

($\sigma_{xy} = 0$) plateaux (ZHPs) between the $\sigma_{xy} = \pm e^2/h$ plateaux of the QAH state (Fig. 1h). Corresponding to the double transitions of σ_{xy} (e^2/h to 0 and 0 to $-e^2/h$), σ_{xx} exhibits two peaks and becomes almost zero between them. These behaviours of σ_{xx} and σ_{xy} directly indicate the formation of the axion insulator (see Supplementary Notes 3 and 4 for further discussion). Although the Cr densities of the two magnetic TI layers are the same, we anticipate that the vertical asymmetry of Cr doping brings about the difference in the magnetic anisotropy between the separated magnetic layers (see also Supplementary Note 3). In the following, we focus on the ZHP state in this asymmetric heterostructure with the thicker separation layer (Fig. 1e).

To clarify the relation between the two quantized states, the ZHP and QAH states, we investigated their dependences on the chemical potential by applying a gate voltage (V_G). Figure 2a shows the magnetic field dependence of σ_{xy} and σ_{xx} at $V_G = 0$, −15 and −20 V. In negative V_G, σ_{xx} in the QAH state gradually deviates from zero and the width of σ_{xy} in ZHPs becomes narrower. We show the V_G dependence of σ_{xy} and σ_{xx} under the QAH state ($B = 0$ T) and the ZHP state ($B = -B_0$) in Fig. 2b,c, respectively. Close to the charge neutrality point, judged from the QAH state, σ_{xx} also takes a minimum value and $\sigma_{xy} \sim 0$ in the ZHP state. Thus, both the QAH state and the ZHP state are stabilized near the charge neutrality point. The narrower V_G range of the ZHP state than that of the QAH state arises from its low stability, the reason for which is discussed later.

We further investigated the ZHPs in the devices with alternative geometries. Two-terminal conductance in the Hall-bar (Fig. 3a) and the Corbino-disk (Fig. 3b) were measured by applying an a.c. voltage (10 μV, 3 Hz). Figure 3c shows the two-terminal conductance (G_{2T}) of the Hall-bar device used in Fig. 2. In the QAH state, the value of G_{2T} (~$0.95e^2/h$) is close to e^2/h due to the presence of the edge states (a slight deviation can be attributed to an additional contact resistance). In the ZHP state around $B = -B_0$ (−0.18 T), on the other hand, G_{2T} becomes zero (to be exact, $G_{2T} < 0.0002e^2/h$), indicating the absence of edge channels connecting the two electrodes due to the quantum confinement effect on the side surface[20,21,24,25]. Furthermore, we conducted a minor loop measurement starting from $B = 2$ T and reversing the magnetic field from $B = -B_0$ (stable ZHP state) to a positive magnetic field. We found that the ZHP state with almost zero conductance is maintained even at $B = 0$ T. This highly stable insulation of the ZHP state is advantageous for detection of the TME effect. Figure 3d shows results of minor and major loop measurements on the Corbino-disk which directly provides σ_{xx} without the tensor calculation needed in the four-terminal measurement. The outline of the loops is consistent with the results of the four-terminal measurement in the Hall-bar (see Supplementary Note 5), implying that almost zero conductivity is realized.

Similar transitions from QAH states to ZHPs have been reported in recent studies using uniformly Cr-doped ultrathin (~5, 6 QL) TI films[9,10], where strong hybridization between top and bottom

© 2017 Macmillan Publishers Limited, part of Springer Nature. All rights reserved.

surface states is anticipated. The transition is interpreted as a topological phase transition of the surface state to a trivial insulator where the magnetization gap becomes smaller than hybridization gap due to the magnetic multi-domain structure around B_c (refs 8–10). Accordingly, the hybridization gap is essential for the occurrence of the ZHPs in their interpretation[10]. However, this interpretation cannot be applied to our observation because the hybridization gap is negligibly small in our 10-nm-thick film, as described below. To evaluate the effect of the possible hybridization gap, we conducted a measurement under in-plane and tilted magnetic fields. Under the in-plane magnetic field, the magnetization of MTI also lies in plane and the magnetization gap disappears. In such a situation, the hybridization gap, if any, would dominate the transport[10,26,27]. Figure 4a shows the magnetic field dependence of σ_{xx} and σ_{xy} under field angles from the normal of the film $\theta = 0$, 79, 85 and 90°. With tilting magnetic field, the QAH and ZHP states are destroyed due to reduction of the magnetization gap by tilting of the magnetization. At $\theta = 90°$, $\sigma_{xy} \sim 0$ and σ_{xx} takes an almost constant value ($\sim 0.5e^2/h$), suggesting disappearance of the energy gap—that is, an absence of the hybridization gap.

In Fig. 4b we plot the values of σ_{xy} and σ_{xx} at $B = 2$ T with variation of θ on the σ_{xy}–σ_{xx} plane[6,28–30], together with the data points obtained from the magnetic field dependence at $\theta = 0°$ (Fig. 1h). The QAH and ZHP states correspond to $(\sigma_{xy}, \sigma_{xx}) = (\pm e^2/h, 0)$ and (0, 0), respectively. In the magnetic-field-driven trace (blue open circles), two semicircles centred at $(\sigma_{xy}, \sigma_{xx}) = (\pm e^2/2h, 0)$ appear. In contrast, the θ-driven trace (red solid circles) does not describe double semicircles and the point $(\sigma_{xy}, \sigma_{xx}) = (0, 0)$ corresponding to the ZHP is not reached. This indicates that the hybridization gap is too small to establish the ZHP state of the hybridization origin (see Supplementary Notes 6 and 7 for experiments on the other films expecting a larger hybridization effect).

To discuss more quantitatively, in Fig. 4c we show the temperature dependence of σ_{xx} in the Corbino-disk under the QAH state at $B = 0$ T (green solid triangles), the ZHP states at $B = -B_0$ (black open circles) and 0 T (blue open circles) from magnetic field dependence (see Supplementary Note 8), and an in-plane ($\theta = 90°$) magnetic field at $B = 2$ T (red solid squares). Under the in-plane magnetic field, where no magnetization gap is expected, σ_{xx} decreases slightly with decreasing temperature, but tends to saturate at around 0.5 e^2/h. This result suggests that the hybridization gap in the MTI heterostructure studied here is small compared to the measurement temperature ($T = 40$ mK). In contrast, in the QAH and ZHP states, σ_{xx} decreases dramatically and becomes zero ($\sigma_{xx} < 0.0002e^2/h$) with lowering temperature. The dependence in the QAH and ZHP states can be ascribed to thermal activated conduction with the respective energy scales of 1.52 K in the QAH state ($B = 0$ T), 0.45 K ($B = -B_0$), and 0.61 K ($B = 0$ T) in the ZHP states. It is to be noted that the ZHP state at $B = 0$ T is more stable than the ZHP state at $B = -B_0$. The observed enhanced stability of the ZHP states at $B = 0$ T may be accounted for by the magnetic stability of the MTI heterostructure. The magnitude of the energy gap in the ZHP state is proportional to the perpendicular component of the magnetic moments. At $B = -B_0$ which is close to one of the two (top- and bottom-layer) coercive fields, the magnetic moments may partly tilt from the original direction, resulting in the reduction of the energy gap on average. Hence, by removing the external magnetic field at $B = 0$ T, the anti-parallel magnetic configuration becomes more stable, as reflected in the slightly higher activation energy.

In conclusion, our magnetotransport study establishes the ZHP state realized by an anti-parallel magnetization in the MTI heterostructure. The stable ZHP state with zero conductivity constitutes the simplest and ideal model for the axion insulator. The magnetic heterostructure engineering in TI represents a step forward for observation of the long-sought TME effect with axion dynamics, and promises future evolution of dissipationless topological electronics.

Methods

Methods, including statements of data availability and any associated accession codes and references, are available in the online version of this paper.

Received 18 June 2016; accepted 11 January 2017; published online 13 February 2017

References

1. Hasan, M. Z. & Kane, C. L. Colloquium: topological insulators. *Rev. Mod. Phys.* **82,** 3045–3067 (2010).
2. Qi, X.-L. & Zhang, S.-C. Topological insulators and superconductors. *Rev. Mod. Phys.* **83,** 1057–1110 (2011).
3. Qi, X.-L., Hughes, T. L. & Zhang, S.-C. Topological field theory of time-reversal invariant insulators. *Phys. Rev. B* **78,** 195424 (2008).
4. Wilczek, F. Two applications of axion electrodynamics. *Phys. Rev. Lett.* **58,** 1799–1802 (1987).
5. Essin, A. M., Moore, J. E. & Vanderbilt, D. Magnetoelectric polarizability and axion electrodynamics in crystalline insulators. *Phys. Rev. Lett.* **102,** 146805 (2009).
6. Nomura, K. & Nagaosa, N. Surface-quantized anomalous Hall current and the magneto electric effect in magnetically disordered topological insulators. *Phys. Rev. Lett.* **106,** 166802 (2011).
7. Mogi, M. *et al*. Magnetic modulation doping in topological insulators toward higher-temperature quantum anomalous Hall effect. *Appl. Phys. Lett.* **107,** 182401 (2015).
8. Wang, J., Lian, B., Zhang, H. & Zhang, S.-C. Universal scaling of the quantum anomalous Hall plateau transition. *Phys. Rev. B* **89,** 085106 (2014).
9. Feng, Y. *et al*. Observation of the zero Hall plateau in a quantum anomalous Hall insulator. *Phys. Rev. Lett.* **115,** 126801 (2015).
10. Kou, X. *et al*. Metal-to-insulator switching in quantum anomalous Hall states. *Nat. Commun.* **6,** 8474 (2015).
11. Brüne, C. *et al*. Quantum Hall effect from the topological surface states of strained bulk HgTe. *Phys. Rev. Lett.* **106,** 126803 (2011).
12. Ren, Z. *et al*. Large bulk resistivity and surface quantum oscillations in the topological insulator Bi_2Te_2Se. *Phys. Rev. B* **82,** 241306 (2010).
13. Zhang, J. *et al*. Band structure engineering in $(Bi_{1-x}Sb_x)_2Te_3$ ternary topological insulators. *Nat. Commun.* **2,** 574 (2011).
14. Haldane, F. D. M. Model for a quantum Hall effect without Landau levels: condensed-matter realization of the 'parity anomaly'. *Phys. Rev. Lett.* **61,** 2015–2018 (1988).
15. Yu, R. *et al*. Quantized anomalous Hall effect in magnetic topological insulators. *Science* **329,** 61–64 (2010).
16. Chang, C.-Z. *et al*. Experimental observation of the quantum anomalous Hall effect in a magnetic topological insulator. *Science* **340,** 167–170 (2013).
17. Chang, C.-Z. *et al*. High-precision realization of robust quantum anomalous Hall state in a hard ferromagnetic topological insulator. *Nat. Mater.* **14,** 473–477 (2015).
18. Morimoto, T., Furusaki, A. & Nagaosa, N. Topological magnetoelectric effects in thin films of topological insulators. *Phys. Rev. B* **92,** 085113 (2015).
19. Wang, J., Lian, B., Qi, X.-L. & Zhang, S.-C. Quantized topological magnetoelectric effect of the zero-plateau quantum anomalous Hall state. *Phys. Rev. B* **92,** 081107 (2015).
20. Fu, H.-H., Lu, J.-T. & Gao, J.-H. Finite-size effects in the quantum anomalous Hall system. *Phys. Rev. B* **89,** 205431 (2014).
21. Morimoto, T., Furusaki, A. & Nagaosa, N. Charge and spin transport in edge channels of a $\nu = 0$ quantum Hall system on the surface of topological insulators. *Phys. Rev. Lett.* **114,** 146803 (2015).
22. Liu, C.-X. *et al*. Oscillatory crossover from two dimensional to three dimensional topological insulators. *Phys. Rev. B* **81,** 041307(R) (2010).
23. Zhang, Y. *et al*. Crossover of the three-dimensional topological insulator Bi_2Se_3 to the two-dimensional limit. *Nat. Phys.* **6,** 584–588 (2010).
24. Wang, J., Lian, B., Zhang, H. & Zhang, S.-C. Anomalous edge transport in the quantum anomalous Hall state. *Phys. Rev. Lett.* **111,** 086803 (2013).
25. Kou, X. *et al*. Scale-invariant quantum anomalous Hall effect in magnetic topological insulators beyond the two-dimensional limit. *Phys. Rev. Lett.* **113,** 137201 (2014).
26. Kandala, A., Richardella, A., Kempinger, S., Liu, C.-X. & Samarth, N. Giant anisotropic magnetoresistance in a quantum anomalous Hall insulator. *Nat. Commun.* **6,** 7434 (2015).
27. Feng, X. *et al*. Thickness dependence of the quantum anomalous Hall effect in magnetic topological insulator films. *Adv. Mater.* **28,** 6386–6390 (2016).

© 2017 Macmillan Publishers Limited, part of Springer Nature. All rights reserved.

28. Checkelsky, J. G. *et al*. Trajectory of the anomalous Hall effect towards the quantized state in a ferromagnetic topological insulator. *Nat. Phys.* **10,** 731–736 (2014).
29. Kivelson, S., Lee, D.-H. & Zhang, S.-C. Global phase diagram in the quantum Hall effect. *Phys. Rev. B* **46,** 2223–2238 (1992).
30. Burgess, C. P., Dib, R. & Dolan, B. P. Derivation of the semicircle law from the law of corresponding states. *Phys. Rev. B* **62,** 15359–15362 (2000).

Acknowledgements

We thank J. Wang, T. Morimoto and N. Nagaosa for fruitful discussions. We thank T. Yokouchi for experimental support. This research was supported by the Japan Society for the Promotion of Science through the Funding Program for World-Leading Innovative R & D on Science and Technology (FIRST Program) on 'Quantum Science on Strong Correlation' initiated by the Council for Science and Technology Policy, JSPS/MEXT Grant-in-Aid for Scientific Research (No. 24224009, 24226002, 15H05867), and CREST, JST.

Author contributions

M.M. and R.Y. grew and characterized the samples. M.M. and M.Kawamura conducted the device fabrication. M.Kawamura, M.M., R.Y. and Y.K. performed transport measurements. N.S. and M.M. conducted magnetization measurements. M.M. and M.Kawamura analysed the data. A.T., K.S.T., M.Kawasaki and Y.T. contributed to discussion of the results and guided the project. Y.T. conceived and coordinated the project.

Additional information

Supplementary information is available in the online version of the paper. Reprints and permissions information is available online at www.nature.com/reprints. Correspondence and requests for materials should be addressed to M.M. or Y.T.

Competing financial interests

The authors declare no competing financial interests.

© 2017 Macmillan Publishers Limited, part of Springer Nature. All rights reserved.

Methods

Thin-film growth. The Cr-modulation-doped $(Bi, Sb)_2Te_3$ thin films were grown by molecular beam epitaxy (MBE) on insulating ($>10^7\,\Omega$ cm) InP(111)A substrates. Before the growth, the substrates were pre-annealed at 380 °C in a growth chamber to clean the surface. The growth temperature was 200 °C. During $(Bi,Sb)_2Te_3$ growth, Bi, Sb and Te were co-evaporated and Cr was selectively supplied. The total flux of Bi and Sb was maintained at 5.0×10^{-6} Pa, as determined from a beam flux monitor, and the ratio of Bi to Sb was carefully chosen for precise control of the chemical potential within the magnetization gap, taking into account its shift due to Cr doping. The Te was over-supplied (the Te/(Bi + Sb) ratio was close to 40) to suppress Te vacancies. Under this condition, the growth rate was about 0.2 nm min^{-1}. After the growth, annealing under exposure to Te was performed *in situ* at 380 °C for 30 min to make a smoother surface. On taking the films out of the MBE chamber, a 3-nm-thick AlO_x capping layer was immediately deposited by atomic layer deposition (ALD) at room temperature to prevent deterioration of the films.

Device fabrication. The Hall-bars and Corbino-disks were patterned by conventional photolithography and Ar ion-milling processes. For electric field control of the chemical potentials, a 30-nm-thick AlO_x dielectric layer was deposited by ALD. For Ohmic-contact electrodes and the top gate electrode, 5-nm-thick Ti and subsequent 45-nm-thick Au were deposited by electron-beam evaporation. The dimension of the Hall-bar is $300 \times 300\,\mu$m. The inner and outer radii of the Corbino-disk are 250 μm and 400 μm, respectively.

Transport measurement. Electrical transport measurements of magnetic TI devices were performed in dilution refrigerators with a standard lock-in technique at low frequency (3 Hz) with low excitations (1 nA for four-terminal measurement and 10 μV for two-terminal measurement) to suppress heating effects. σ_{xy} and σ_{xx} in the four-terminal measurements were converted from ρ_{yx} and ρ_{xx} following the tensor relations $\sigma_{xy} = \rho_{yx}/(\rho_{xx}^2 + \rho_{yx}^2)$ and $\sigma_{xx} = \rho_{xx}/(\rho_{xx}^2 + \rho_{yx}^2)$.

Data availability. All relevant data within this paper are available from the authors upon reasonable request.

© 2017 Macmillan Publishers Limited, part of Springer Nature. All rights reserved.